ORIGINAL ARTICLE

Seasonality of interannual atmosphere–ocean interaction in the South China Sea

Zhuoqi He · Renguang Wu

Abstract The present study documents the atmosphere–ocean interaction in interannual variations over the South China Sea (SCS). The atmosphere–ocean relationship displays remarkable seasonality and regionality, with an atmospheric forcing dominant in the northern and central SCS during the local warm season, and an oceanic forcing in the northern SCS during the local cold season. During April–June, the atmospheric impact on the sea surface temperature (SST) change is characterized by a prominent cloud-radiation effect in the central SCS, a wind-evaporation effect in the central and southern SCS, and a wind-driven oceanic effect along the west coast. During November–January, regional convection responds to the SST forcing in the northern SCS through modulation of the low-level convergence and atmospheric stability. Evaluation of the precipitation–SST and precipitation–SST tendency correlation in 24 selected models from CMIP5 indicates that the simulated atmosphere–ocean relationship varies widely among the models. Most models have the worst performance in spring. On average, the models simulate better the atmospheric forcing than the oceanic forcing. Improvements are needed for many models before they can be used to understand the regional atmosphere–ocean interactions in the SCS region.

Z. He
Institute of Space and Earth Information Science, The Chinese University of Hong Kong, Shatin, New Territories, Hong Kong

R. Wu (✉)
Department of Physics, Institute of Space and Earth Information Science, The Chinese University of Hong Kong, Fok Ying Tung Remote Sensing Science Building, Shatin, New Territories, Hong Kong
e-mail: renguang@cuhk.edu.hk

1 Introduction

The South China Sea (SCS), bordered by the Asian continent, the Malay Peninsula, Borneo, and the Philippine Islands, is the largest marginal sea in the western North Pacific, with a mean depth of 1,800 m (Twigt et al. 2007). As a part of tropical eastern Indian Ocean–western Pacific warm pool and the Asian monsoon region, the SCS displays remarkable air–sea interaction on different time scales (Wang et al. 1997; Wu and Wang 2001; Wu 2002, 2010; Liu et al. 2004; Lestari et al. 2011; Roxy and Tanimoto 2012; Wu et al. 2012; He and Wu 2013). These air–sea interactions are related to climate variability in the surrounding regions. For example, during the SCS summer monsoon onset, sea surface temperature (SST) warming induces convection by modifying the atmospheric instability and lower-level convergence; in turn, the convection feeds back negatively on the SST by surface heat flux anomalies associated with surface wind and cloud changes (Wu 2002, 2010). The SST cooling in the SCS is conducive to a reversal of the east–west SST gradient between the SCS and the Philippine Sea, which favors the eastward advance of the summer monsoon (Wu and Wang 2001; Wu 2002). Thus, understanding the atmosphere–ocean interaction in the SCS and its roles in regional climate is critical for regional climate prediction and climate-related risk management.

The atmospheric changes influence SST by cloud-radiation effect, wind-evaporation effect, and wind-induced oceanic processes (Lau and Nath 2003; Wu and Kirtman

2007). Anomalous atmospheric convection associated with enhanced (reduced) cloudiness can cool (warm) the ocean mixed layer by modifying the incoming shortwave radiation (Klein et al. 1999). The change in surface latent heat flux associated with surface wind speed and sea–air humidity difference is another important factor for the SST anomalies (Klein et al. 1999; Wu and Kinter III 2010). Moreover, anomalous wind-driven ocean advection and upwelling can contribute to the SST change (He and Wu 2013). On the other hand, SST change can modify regional convection through lower-level moisture convergence, surface evaporation and lower tropospheric stability (Lindzen and Nigam 1987; Wu and Wang 2000). This local SST impact on atmospheric convection is reflected in the precipitation–SST relationship, and the atmospheric impact on SST is indicated in the precipitation–SST tendency relationship (Wu et al. 2006; Wu and Kirtman 2007). For example, given a positive SST anomaly, surface atmospheric pressure decreases due to the warming of the atmospheric column through upward turbulent surface heat fluxes. The induced lower-level convergence and the destabilizing of the lower troposphere favor more convection and precipitation. Due to the fast atmospheric response, this SST impact on precipitation is captured in a positive simultaneous precipitation–SST correlation. Given above-normal precipitation, which is associated with more cloud and active disturbance, the downward shortwave radiation likely decreases and upward surface evaporation increases. The surface heat flux input into the ocean is thus reduced, leading to a decrease of SST. This atmospheric impact on the SST change is manifested in the simultaneous precipitation–SST tendency correlation.

The air–sea interaction on interannual time scales has been discussed in large ocean basins, such as the tropical Indo-western Pacific (Lau and Nath 2003; Wang et al. 2003; Wu and Kirtman 2007; Wu et al. 2008, 2011), mid-latitude North Pacific (Norris et al. 1998; Wu and Kinter III 2010), and tropical North Atlantic (Wu and Kirtman 2011). There have been several previous studies of the interannual variations in the SCS. An interannual oscillation in the air–sea system in the SCS was demonstrated by Wang et al. (1997) based on the relationship between SST and surface wind. The lower-level meridional wind anomalies, which are induced by the longitudinal SST gradient, in turn, feed back to SST through advection and latent heat flux transportation. Xie et al. (2003) pointed out that the wind-induced cold filament off the coast of South Vietnam is an important player in interannual variability in the summer SCS by analyzing the case in 1998, when a diminished wind jet offshore resulted in the disappearance of the cold filament and led to great summer warming associated with suppressed mid-summer cooling. Liu et al. (2004) demonstrated that a winter cold tongue in the SCS displays

considerable interannual variability associated with El Niño-Southern Oscillation (ENSO). In an El Niño event, the SCS ocean circulation spins down with weakened monsoons and results in a warming in the cold tongue. Wang et al. (2006a) showed that the atmospheric changes associated with El Niño events can influence surface heat fluxes and oceanic flows that further warm or cool the SCS. The shortwave radiation and latent heat flux anomalies are major contributions to the SST anomalies in February, and the mean meridional geostrophic heat advection makes the SST anomalies peak again in August. Using a coupled general circulation model (CGCM), Lestari et al. (2011) demonstrated that the absence of the air–sea coupling keeps SST warm in the SCS and increases the local precipitation, which suggests that the air–sea coupling works to stabilize the monsoon and hence suppress the variability via the large-scale moisture transport and the wind-induced local evaporation.

These previous studies are either based on specific regions or individual seasons. For example, Xie et al. (2003) only analyzed coastal Vietnam in the 1998 summer; Liu et al. (2004) focused on the cold tongue of the SSCS in winter; Lestari et al. (2011) were only concerned with summer monsoon season; Wang et al. (2006a) addressed the influence of atmospheric changes on SST, but did not consider the impact of SST change on the atmosphere. There is a lack of systematic investigation of the seasonality and regionality of the local air–sea interaction in the SCS. Does the atmosphere–ocean interaction in summer perform the same as in winter? How does the SST influence the regional precipitation differently between the southern and northern SCS? These issues remain to be addressed. Unlike the previous studies, the present study considers both the atmospheric and oceanic forcing processes and compares their differences in different seasons and regions.

Apart from the observational data, there are more and more model simulations applied in the studies of air–sea interaction. The WCRP's Working Group on Coupled Modelling agreed on a new set of coordinated climate model experiments, which comprises the phase five of the Coupled Model Intercomparison Project (CMIP5). The CMIP5 includes simulations for the IPCC AR5 and provides a framework for coordinated climate change experiments (Taylor et al. 2011, 2012). The model simulation is an approach to understand the physical process connecting the atmosphere and the ocean. Previous evaluations have been done for several individual models (Trenberth and Shea 2005; Wu et al. 2006) and over the global domain (Wu et al. 2013). However, the capability of these global models to reveal the regional processes of air–sea interaction still remains unknown. The models should be evaluated before the model simulations are applied in the

studies of regional air–sea interactions. Given the availability of the new version of climate model simulations, the present study will evaluate the model performance of air–sea relationship in the SCS.

The text is organized as follows. The datasets and methods are described in Sect. 2. In Sect. 3, we discuss the seasonal evolution of atmosphere–ocean relationship. The cases of atmospheric and oceanic forcing processes are addressed in Sect. 4. Section 5 presents the evaluation of the model performances of the atmosphere–ocean relationship against observations. A summary and discussion are provided in Sect. 6.

2 Datasets and methods

The National Oceanic and Atmospheric Administration (NOAA) optimum interpolation (OI) version 2 monthly mean SST (Reynolds et al. 2002) is used in the present study. This SST dataset is available from December 1981 to May 2013 on a $1° \times 1°$ grid. Global Precipitation Climatology Project (GPCP) version 2.2 monthly precipitation dataset (Adler et al. 2003; Huffman et al. 2009) is used. The GPCP dataset is on $2.5° \times 2.5°$ global grids and covers the period of January 1979–February 2013.

Monthly mean wind, relative humidity, and air temperature from the NCEP-DOE Reanalysis 2 are used in this study (Kanamitsu et al. 2002). This dataset is available from January 1979 to December 2012 with a resolution of $2.5° \times 2.5°$. Monthly mean net surface shortwave radiation, net surface longwave radiation, latent heat fluxes, and sensible heat fluxes from the Woods Hole Oceanographic Institute (WHOI) Objectively Analyzed Air–sea Fluxes (OAFlux) (Yu et al. 2008) is used. This dataset covers the period from July 1983 to December 2009 on a $1° \times 1°$ grid.

Monthly ensemble means of v.2.0 of Geophysical Fluid Dynamics Laboratory (GFDL) ocean data assimilation product available from 1979 to 2008 is used in the present study (Griffies et al. 2004). The ocean component of the coupled data assimilation (CDA) is configured with 50 vertical levels (22 levels of 10-m thickness each in the top 220 m) and $1°$ horizontal B-grid resolution, telescoping to $1/3°$ meridional spacing by $1°$ near the equator.

The present study uses monthly mean precipitation and skin temperature from 24 CMIP5 models, which are available at http://pcmdi9.llnl.gov/. More than 20 modeling groups perform CMIP5 simulations using more than 50 models (Taylor et al. 2011, 2012). Because of the large number of simulations included in the CMIP5 framework, only one member for each of 24 model outputs from the historical simulations is analyzed in the present study. The historical simulations cover more than 100 years up to 2005. and the calculation in the present study is based on a common period from 1982 to 2005 for a fair comparison with the observations. The information for the models selected is given in Table 1.

The interannual atmosphere–ocean relationships are inferred by correlation and regression derived from monthly means anomalies. The climatology of the observation and the model data are estimated based on the period of 1984–2007 and the period of 1982–2005, respectively. The SST tendency is calculated using centered differencing, i.e., the SST tendency in a specific month is calculated as the difference of the SST in the succeeding month minus the SST in the preceding month divided by 2 (Wu and Kirtman 2007; He and Wu 2013). All the variables are converted to $1°$ resolution using a linear interpolation.

The atmosphere–ocean relationship in observations is documented based on the simultaneous precipitation–SST and precipitation–SST tendency correlations, following Wu et al. (2006) and Wu and Kirtman (2007). The precipitation–skin temperature (P–ST) and precipitation–skin temperature tendency (P–STn) correlations in models are evaluated to understand the model deficiency in simulating the atmosphere–ocean relationship. Note that we used the skin temperature for model output in view of the availability. Since we are concerned with the interannual anomalies, the systematic differences between skin temperature and SST are expected to be largely reduced and thus not affect our results.

3 Seasonal evolution of atmosphere–ocean relationship

In this section, we discuss the seasonality of the atmosphere–ocean relationship starting with comparison of the simultaneous precipitation–SST and precipitation–SST tendency correlations. Figure 1 shows the point-wise contemporaneous precipitation–SST and precipitation–SST tendency correlation in four seasons: spring (March–May, MAM), summer (June–August, JJA), autumn (September–November, SON), and winter (December–February, DJF) for the period of 1984–2007.

The precipitation–SST correlation (Fig. 1a–d) displays a noticeable seasonal change in the SCS. In summer, a high negative precipitation–SST correlation appears in the northern SCS with a magnitude over 0.4, and a weak positive correlation is observed in the far southern SCS. In winter, the correlation pattern tends to be opposite to that in summer, with a strong positive precipitation–SST relationship in the northern SCS and a negative one in the southern SCS with the maximum correlation exceeding 0.3. In spring, there is a significant negative correlation in the southwestern SCS. In autumn, a positive correlation is

Table 1 Information of the 24 climate models used in the model evaluation

Institute	Model	Version	Horizontal resolution (grid numbers)
CCCMA	CanCM4	20120207	128 × 64
CCCMA	CanESM2	20120718	128 × 64
CNRM-CERFACS	CNRM-CM5	20110701	256 × 128
IMM	inmcm4	20111201	180 × 120
ISPL	ISPL-CM5A-LR	20110406	96 × 96
ISPL	ISPL-CM5A-MR	20111119	144 × 143
ISPL	ISPL-CM5B-LR	20120114	96 × 96
MIROC	MIROC4h	20110729	640 × 320
MIROC	MIROC5	20111104	256 × 128
MIROC	MIROC-ESM	20110929	128 × 64
MIROC	MIROC-ESM-CHEM	20111004	128 × 64
MOHC	HadCM3	20110823	96 × 73
MOHC	HadGEM2-CC	20110927	192 × 145
MOHC	HadGEM2-ES	20110329	192 × 145
MPI-M	MPI-ESM-LR	20120315	192 × 96
MPI-M	MPI-ESM-MR	20120503	192 × 96
MPI-M	MPI-ESM-P	20120315	192 × 96
MRI	MRI-CGCM3	20110831	320 × 160
NCAR	CCSM4	20120213	288 × 192
NCC	NorESM1-M	20120412	144 × 96
NCC	NorESM1-ME	20120402	144 × 96
NOAA-GFDL	GFDL-CM3	20120227	144 × 90
NOAA-GFDL	GFDL-ESM2G	20120412	144 × 90
NOAA-GFDL	GFDL-ESM2M	20111228	144 × 90

Project: CMIP5; experiment: historical; time_frequency: month; modeling realm: atmosphere

seen in the northeastern SCS and a negative correlation is along the coast of Malay Peninsula.

In contrast to the precipitation–SST correlation, a negative precipitation–SST tendency correlation prevails in the central SCS during the four seasons (Fig. 1e–h). A negative correlation is also observed in the northern SCS from spring to summer and in the southern SCS from autumn to winter. The negative precipitation–SST tendency correlation reaches a magnitude larger than 0.4 in the central SCS, with the strongest correlation in autumn (Fig. 1g). In winter, a positive precipitation–SST tendency correlation appears in the far northern SCS (Fig. 1h).

In winter, the northern SCS displays the strongest positive precipitation–SST correlation (Fig. 1d) accompanied by a relatively weak positive precipitation–SST tendency correlation (Fig. 1h). This indicates that an oceanic forcing is dominant in this region during winter, with a negligible influence of atmosphere on SST. In contrast, in summer, the northern SCS is under the influence of negative correlation in both precipitation–SST and precipitation–SST tendencies (Fig. 1b, f). This implies a control of atmospheric impact on SST during summer. The atmospheric impact is also expected in the northern SCS during spring and the central SCS during autumn.

To address in detail the seasonal evolution of the air–sea relationship in different regions, we display in Fig. 2 the simultaneous precipitation–SST and precipitation–SST tendency correlation calculated for individual months based on averaged quantities over the region of 14–20°N and 110–120°E (denoted as northern SCS or NSCS), 8–14°N and 110–118°E (denoted as central SCS or CSCS), and 2–8°N and 104–115°E (denoted as southern SCS or SSCS), respectively. Obvious seasonality can be identified in the variations of both the sign and magnitude of the correlation.

In the NSCS (Fig. 2a), the largest negative precipitation–SST tendency correlation is seen from April to June. In the other months, the precipitation–SST tendency correlation is not significant. The largest positive precipitation–SST correlation appears in November–December and a negative correlation is seen in June–August. The above seasonal change in the precipitation–SST and precipitation–SST tendency correlation suggests different types of atmosphere–ocean relationship in different seasons. In the CSCS (Fig. 2b), the magnitude of the precipitation–SST tendency correlation is larger than that of the precipitation–SST correlation in most of the months. There are two periods during which the negative precipitation–SST tendency correlation is high: April–June and September–
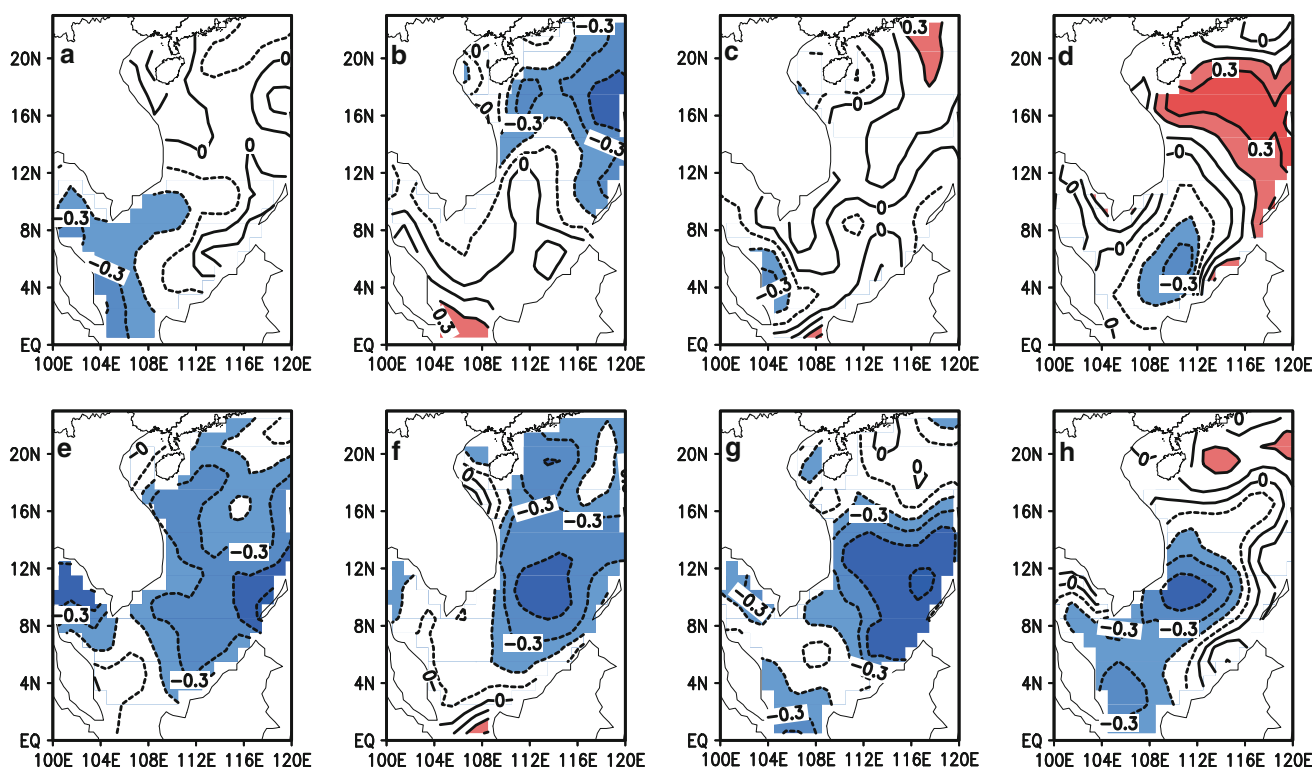
Fig. 1 Point-wise and simultaneous precipitation–SST (on the *top*) and precipitation–SST tendency correlation (on the *bottom*) in **a**, **e** MAM, **b**, **f** JJA, **c**, **g** SON, and **d**, **h** DJF for the period of 1984–2007. The contour interval is 0.1. *Shaded regions* indicate that the correlations are statistically significant at the 90 % confidence level

December. The precipitation–SST correlation is weak and insignificant in most of the months. In the SSCS (Fig. 2c), the precipitation–SST correlation is weaker than the precipitation–SST tendency correlation in most of the months, which is similar to the CSCS. Significant precipitation–SST tendency correlation is seen in some months as well. One noticeable period is around August during which a moderate positive precipitation–SST correlation concurs with a moderate negative precipitation–SST tendency correlation. This feature suggests that there may be both atmospheric forcing and oceanic forcing during August. However, the correlation coefficient is not so high, indicating that this signal is not very robust.

The spatial distributions of the precipitation–SST and precipitation–SST tendency correlations and their seasonal change indicate that the air–sea interaction in the SCS has distinct regimes depending on the season and region. The alternative dominance of different regimes of air–sea interaction will be demonstrated in the next section by selecting different cases.

4 Atmospheric and oceanic forcing cases

Based on the simultaneous precipitation–SST and precipitation–SST tendency correlation discussed in Sect. 3, we address separately the atmospheric forcing of ocean (Sect. 4.1) by selecting the case in the CSCS during April–June (AMJ), and the oceanic forcing of atmosphere (Sect. 4.2) by using the case in the NSCS during November–January (NDJ). Regression analysis is performed in this section to estimate the magnitude of anomalies.

4.1 Atmospheric forcing case

According to the heat budget equation of the mixed layer (Formula 1; He and Wu 2013), the change of SST (SST tendency) is primarily determined by the dynamic process of interior ocean (advection and upwelling), and the net heat flux including short wave radiation (SW), long wave radiation (LW), latent heat flux (LHF), and sensible heat flux (SHF):

$$\frac{\partial T}{\partial t} = \frac{(\text{SW} - \text{SWpen}) - \text{LHF} - \text{LW} - \text{SHF}}{\rho c_{\text{p}} h} - \overline{\vec{V} \cdot \nabla T}$$
$$- \overline{w \frac{\partial T}{\partial z}}. \qquad (1)$$

Here, ρc_{p} is the specific heat capacity per unit volume, h is the mixed layer depth (MLD) which is defined as the depth of the level where the ocean temperature difference from
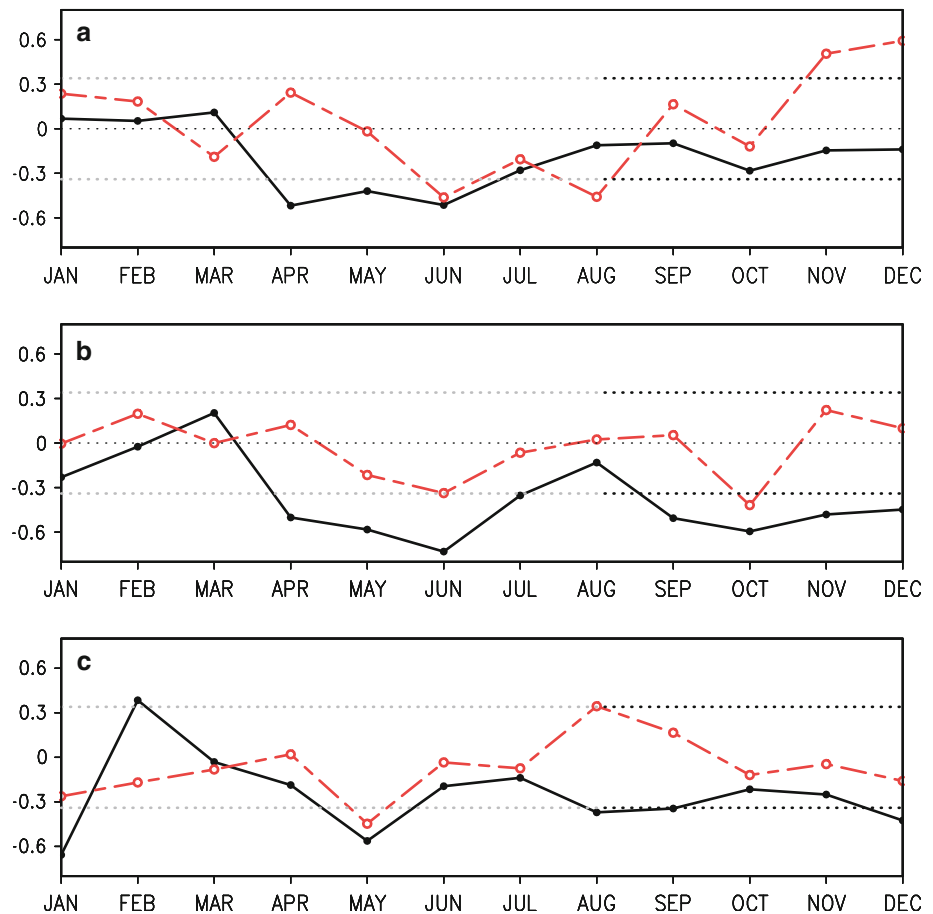
the SST equals to 0.5 °C, T is the ocean temperature within the mixed layer that is well represented by SST and thus is replaced by SST on the left side of the equation, $\overrightarrow{V} \cdot \nabla T$ is the horizontal advection averaged in the mixed layer, $\overline{w \frac{\partial T}{\partial z}}$ is the vertical advection averaged in the mixed layer, which is approximately equivalent to the effect of vertical entrainment at the base of the mixed layer, LHF is latent heat flux, LW is net long wave radiation, SHF is sensible heat flux, SW is net surface shortwave radiation, and SWpen is the shortwave radiation penetration through the depth h and is calculated following the solar radiation penetration parameterization scheme (Paulson and Simpson 1977) used by He and Wu (2013). The horizontal and vertical advections in the mixed layer are calculated as

$$\overline{()} = \frac{1}{h} \int_{-h}^{0} ()\mathrm{d}z. \tag{2}$$

In the following discussion, for a better description of the atmospheric impacts on the SST change, we particularly focus on the factors including SW (SWpen included), LHF, ocean horizontal advection, and vertical

advection (upwelling), which are the major contributions to the SST tendency. For convenience of comparison between different heat fluxes, oceanic terms, and the SST tendency, the convention used for heat fluxes, ocean vertical upwelling, and ocean horizontal advection is positive when they contribute positively to the SST increase. The net heat flux (Fig. 3b) and oceanic terms (Fig. 3c, d) have been converted to the same unit as the SST tendency (K/month).

As discussed in Sect. 3, the typical atmospheric forcing is revealed in both the NSCS and CSCS from April to June and the SSCS in December–January. In the following, we present analyses of the CSCS case. The NSCS case (figures not shown) displays results similar to those in the CSCS case. Figure 3 shows the regression map with respect to normalized AMJ SST tendency averaged in the CSCS.

The SST tendency anomalies (Fig. 3a) display a same-sign change in the whole SCS. The net heat flux (Fig. 3b) makes significant contributions to the SST tendency from the central SCS to the southern SCS, explaining more than 50 % of the SST tendency. In the western region, the ocean upwelling (Fig. 3d) has a positive contribution of about 1/2 of the SST tendency, while in the eastern SCS, the ocean vertical upwelling has a weak negative contribution to the
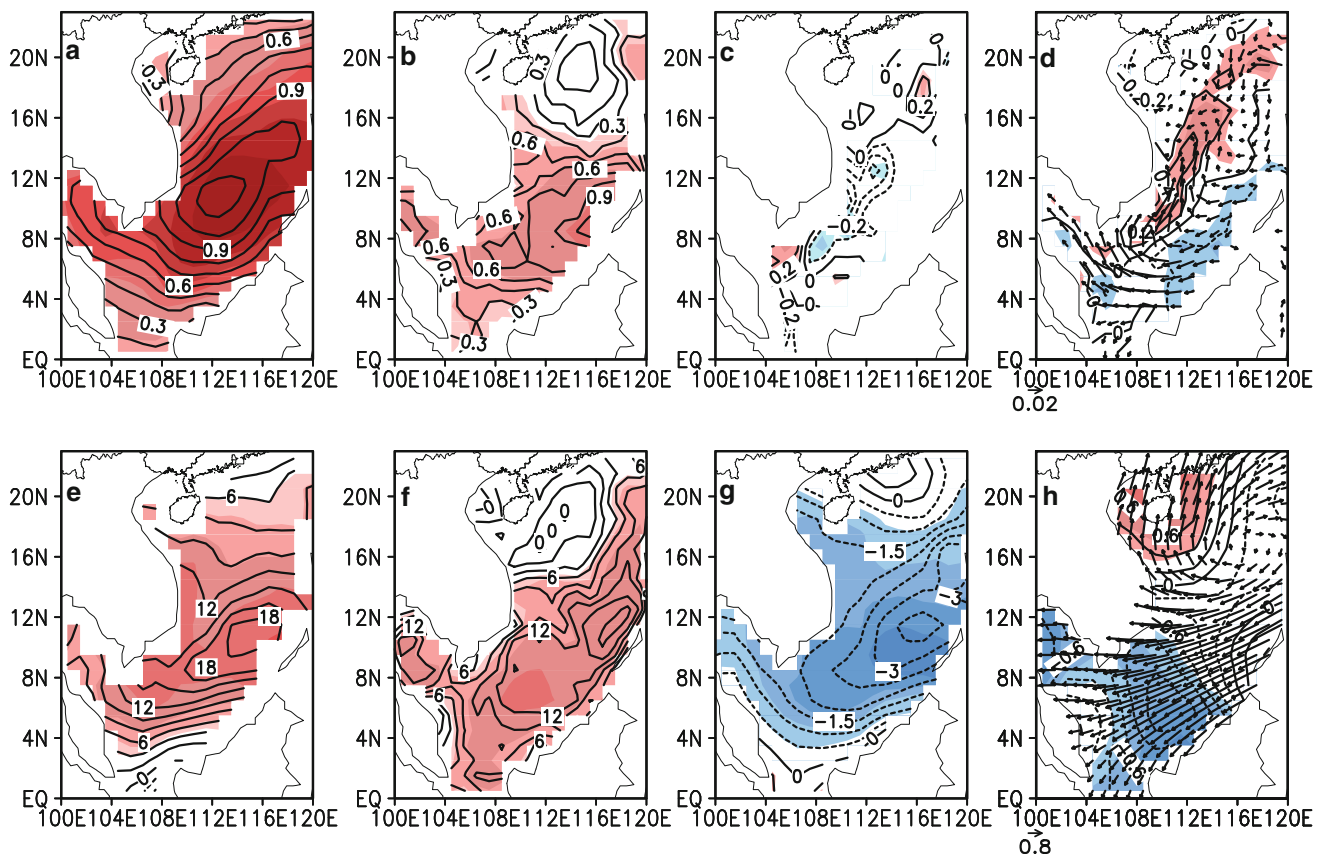
Fig. 3 Simultaneous regression with respect to normalized AMJ SST tendency in the CSCS for the period of 1984–2007. **a** SST tendency (K/month), **b** net heat flux/MLD (SWpen included, K/month), **c** ocean horizontal advection (K/month), **d** ocean current (m/s) and upwelling (*contour*, K/month), **e** short wave radiation (SWpen included, W/m²), **f** latent heat flux (downward positive, W/m²), **g** precipitation (mm/day), and **h** surface wind vector (*contour lines* stand for wind speed, m/s). *Shaded regions* indicate that the correlations are statistically significant at the 90 % confidence level

SST tendency. The feature of ocean horizontal advection (Fig. 3c) is unclear due to the low-resolution data with undefined grids, and yet it is inferred to be important along the coast regions.

To understand different processes relevant to heat fluxes and oceanic terms, we discuss the regression maps displayed in Fig. 3e–h. For the given positive SST tendency anomalies, the incoming SW (Fig. 3e), as the largest component of net heat flux, is enhanced consistently in the whole region, owing to suppressed cloudiness associated with less precipitation (Fig. 3g), and thus makes a positive contribution to the SST tendency. Due to the reduced surface wind speed associated with anomalous northeasterly winds in the central and southern SCS (Fig. 3h), the outgoing LHF (Fig. 3f) is reduced and thus contributes positively to the SST tendency. Furthermore, the wind-driven oceanic process is also noticeable. As an anomalous anti-cyclonic circulation (Fig. 3h) occurs over the SCS with the center located at 16°N, northeasterly wind anomalies prevail south of 14°N (Fig. 3d). This induces northward (northwestward) Ekman current anomalies,

leading to a significant anomalous downwelling (upwelling) along the southwestern (southeastern) coasts of the SCS. Moreover, Ekman pumping due to wind stress curl also contributes to downward (upward) vertical advection anomalies in the central-northern (southeastern) SCS (figure not shown). This suppresses (enhances) vertical ocean mixing and favors the SST warming (cooling) in the west (east) region.

4.2 Oceanic forcing case

As discussed in the last part, the SST is capable of responding to atmospheric forcing through cloud-radiation, wind-evaporation, and wind-driven oceanic effects. On the other hand, the SST anomalies can modify regional precipitation through modulating the lower-level convergence and atmospheric stability (Lindzen and Nigam 1987; Wu and Wang 2000). This oceanic forcing may play a dominant role in specific seasons and regions. To demonstrate the oceanic forcing, the case in the NSCS from November to January is discussed in this section.

Figure 4 shows the regression map with respect to normalized NDJ SST in the NSCS. The stability parameter is defined as the difference of pseudo-equivalent potential temperature between 1000 and 700 hPa with a negative difference indicating stable lower atmosphere (Roxy and Tanimoto 2007; Wu 2010; He and Wu 2013). Positive SST anomalies (Fig. 4a) appear in both the northern SCS and the western North Pacific with a decrease in the magnitude of the SST anomalies from west to east. In accordance with the SST anomaly distribution, southerly wind anomalies form over the SCS with a cyclonic curvature (Fig. 4d). The wind speed features a decrease from south to north, indicating anomalous lower-level convergence over the central and northern SCS. In contrast, an anomalous lower-level anti-cyclonic circulation forms over the western North Pacific (Fig. 4d). The lower-level anomalous convergence matches well with the above-normal precipitation over the northern SCS (Fig. 4b). This supports the impact of warm SST anomalies on convection through modulating lower-level convergence. Another way through which the SST anomalies affect the atmospheric precipitation is evaporation (Figures not shown). Analysis shows positive evaporation anomalies over the NSCS. These anomalies, however, are not so significant.

SST anomalies can also contribute to precipitation change by affecting the atmospheric stability. An unstable lower troposphere provides favorable conditions for enhancing regional convection. This is supported by distribution of the lower-level atmospheric stability parameter. Overlying the large positive SST anomalies in the SCS (Fig. 4a), a zone of remarkable positive lower-level atmospheric stability anomalies extend from the SCS to the Philippine Sea along 10–20°N (Fig. 4c).

5 Evaluation of the model performance

In this section, we analyze the CMIP5 model performance of precipitation–temperature relationship to provide information about the model's capability of simulating the air–sea relationship in the SCS. Based on the observational analysis in Sect. 3, we particularly focus on the model performance of P–ST correlation during winter and P–STn correlation during summer. Only one member of 24 model outputs from the historical experiments of the CMIP5 simulations is analyzed in the present study. We note that the resolution differs among the models (Table 1).

In this study, we are concerned about the regional air–sea interaction on the interannual scale. Here, how well the

Fig. 4 Simultaneous regression with respect to normalized NDJ SST in the NSCS for the period of 1984–2007. **a** SST (K), **b** precipitation (mm/day), **c** stability parameter (Θe difference between 1000 and 700 hPa, K), **d** wind vector (m/s) and divergence (10^{-6}/s) at 850 hPa. *Shaded regions* indicate that the correlations are statistically significant at the 90 % confidence level
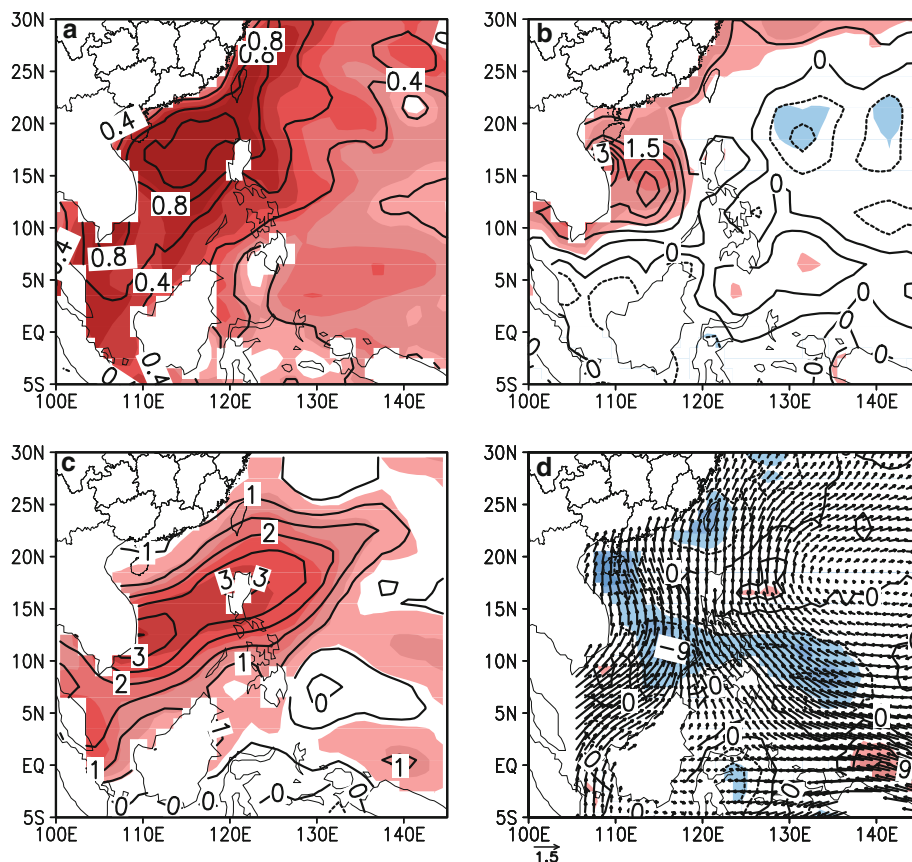
models reproduce precipitation–SST and precipitation–SST tendency relationship in the SCS in the seasonal change is only briefly described (figures not shown). Overall, the model simulations capture reasonably the precipitation–SST and precipitation–SST tendency relationship in the seasonal change. For example, higher (lower) SST from May to August (January–February) is followed by negative (positive) precipitation departure during June–September (February–March). When the precipitation got its minimum (maximum), the SST tendency reaches its maximum (minimum) in March–April (October–November). In comparison, the simulations of the air–sea relationship are better from January to June than from July to December.

The Taylor diagram is used in this study to quantify the overall correspondence between the modeled and observed behavior. The spatial correlation coefficient, the ratio of the standard deviations (RSD) of the modeled and observed fields ($\frac{observedSD}{modeled\ SD}$), and the root-mean-square (RMS) difference between the two patterns (related to the spatial correlation and the standard deviations through the Law of Cosine and it is not plotted in this study) are indicated by a single point on the Taylor diagram. The model points are

plotted based on the spatial correlation and the RSD with respect to the observation. There is a better performance of the model in the P–ST (P–STn) correlation if there is a shorter distance between the modeled and observed points with a higher correlation coefficient. According to these statistics, we can distinguish how accurately a model simulates the natural system. More details about the Taylor diagram can be found in Taylor (2001).

Considering that there are significant precipitation–SST correlations with negative values in JJA and positive values in DJF, and there are significant precipitation–SST tendency correlations throughout the year in observations (Fig. 1), we show in Fig. 5 the normalized pattern statistics describing the P–ST correlations simulated by 24 models in summer and winter, and in Fig. 6 the model performance of P–STn correlations in all the four seasons over the SCS. The observed one is calculated based on GPCP precipitation and OI version 2 SST (refer to Fig. 1). The reference field representing the observed state is plotted along the abscissa with the RSD of 1. The radial distances from the origin to the points are equal to the RSD, the azimuthal positions are determined by the correlation coefficient between the modeled and observed fields, and the distances

Fig. 5 Normalized pattern statistics describing the **a** JJA, **b** DJF precipitation–SST correlation over SCS simulated by 24 models compared with the observation (plotted along the abscissa with the RSD of 1). The radial distances from the origin to the model points are the ratio of the standard deviations; the azimuthal positions are determined by the correlation coefficient between the modeled and observed fields
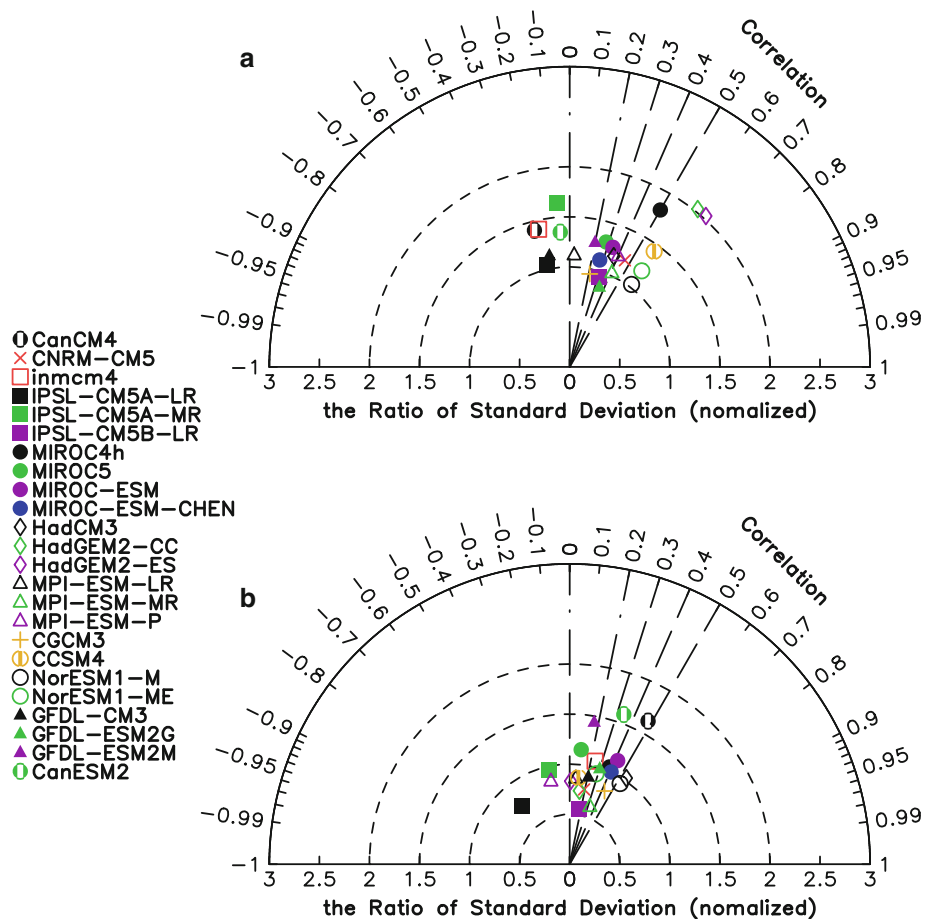
from the model points to the reference point indicate the RMS errors.

The model points of P–ST correlation display a wide range of differences among the models (Fig. 5). The seasonal dependence of the model performance is also obvious. In comparison, higher consistency between model simulations and observations appears in autumn when most of the models have a pattern correlation around 0.4 (not shown). In winter, the RSD tends to be the lowest in most models (Fig. 5b). Spring appears to be the worst season when most of the models display a low pattern correlation and a large RSD (not shown). In summer, the model simulated pattern correlation varies largely from −0.2 to 0.65 though the RSD is close to 1 in most models (Fig. 5a). Since the oceanic forcing discussed in Sects. 3 and 4 is dominant in the SCS during winter, it is worthwhile to examine the performance of individual models in the P–ST correlation. In DJF (Fig. 5b), the HadCM3 model from MOHC and the NorESM1-M model from NCC display the highest pattern correlation of 0.54 and a RSD closest to 1, while the ISPL-CM5A-LR and ISPL-CM5A-MR models from ISLP and the MPI-ESM-P model from MPI-M perform poorly with the lowest pattern correlation from −0.5 to −0.2.

The P–STn correlation also shows differences among the models (Fig. 6), but to a lesser extent compared to the P–ST correlation. The model performance in the P–STn correlation also displays strong seasonality, but this feature is relatively weaker than that seen in the P–ST correlation. In comparison, the model P–STn correlation pattern is closest to observations in autumn (Fig. 6c) with a relatively high pattern correlation of 0.45 on average. The worst model performance in the P–STn correlation appears in spring (Fig. 6a). The performance in summer (Fig. 6b) and winter (Fig. 6d) is between spring and autumn. Another feature to note in Fig. 6 is that the models exaggerate the spatial variability in spring and autumn with the RSD generally larger than 1.0 (Figs. 6a, c), and underestimate the spatial variability in winter with the RSD from 0.5 to 1 (Fig. 6d). In summer, when the atmospheric forcing is demonstrated to play a dominant role in the SCS, the models show a wide range of RSD from 0.7 to 1.8 (Fig. 6b). The MPI-ESM-P model from MPI-M, which shows a poor performance in winter P–ST correlation, displays the highest pattern correlation of 0.6 and the best RSD of 1 in the summer P–STn correlation, while the MIROC5 model from MIROC shows the worst performance with the pattern correlation of 0.

Overall, by comparing Figs. 5 and 6, the models simulate the P–STn correlation better than the P–ST correlation in four seasons with higher pattern correlations on average and fewer differences among models (spring and autumn not shown in Fig. 5). This indicates that the models may be more capable of revealing the atmospheric forcing than the
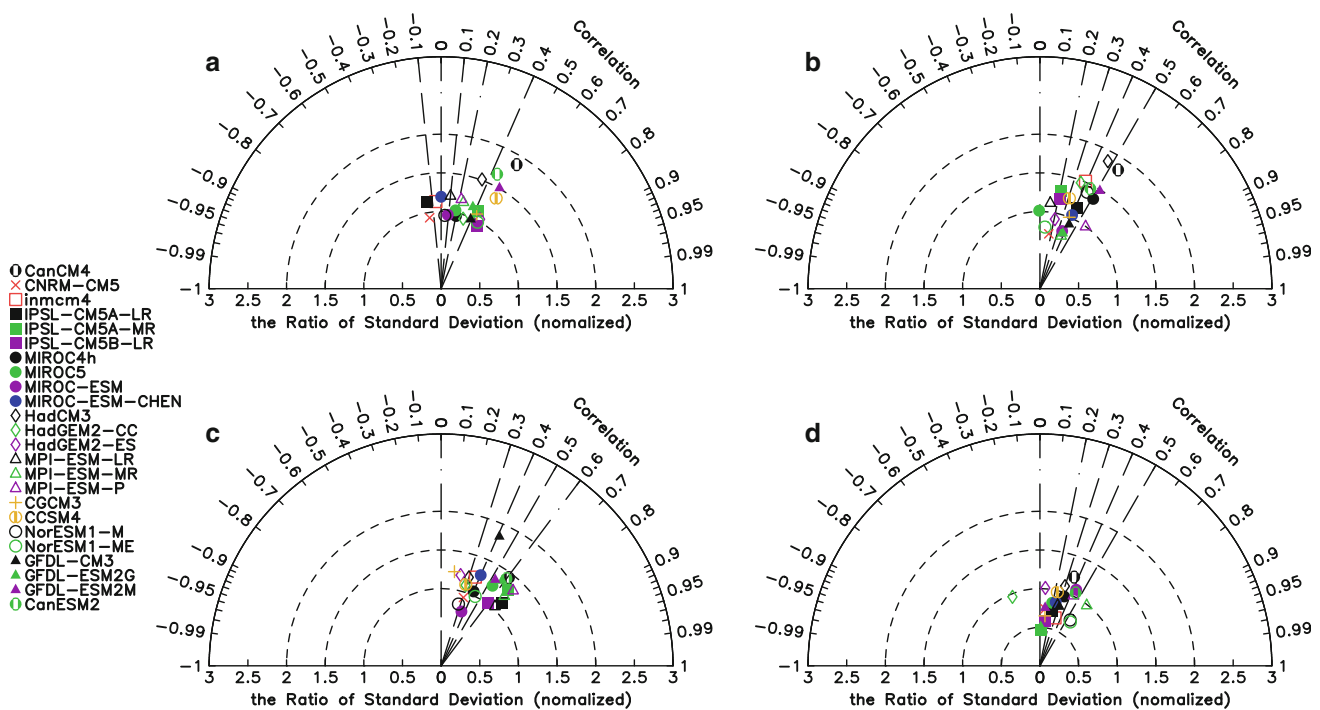

Fig. 6 The same as Fig. 5, but for the precipitation–SST tendency correlation in **a** MAM, **b** JJA, **c** SON, **d** DJF

oceanic forcing process in the SCS. Considering the importance of the P–ST correlation in winter and the P–STn correlation in summer, the models from MIROC institute (except for the MIROC5 model) and CCCMA institute have relatively stable performance with approximately high correlations and RSD close to the reference. Other models to be noted are those from ISPL. They perform relatively well in summer P–STn correlation with an average pattern correlation of 0.3, but display a poor performance in winter P–ST correlation from 0.1 to −0.3. This indicates that ISPL models have difficulty in capturing the oceanic forcing in the SCS. From the above discussion, it can be concluded that there are obvious differences of simulations among models in the same season and that the model performances are unstable with strong seasonality.

To examine the model performance in detail, we further display the distributions of DJF P–ST and JJA P–STn correlations in Fig. 7 by selecting two models for comparison. One is the HadCM3 from MOHC with a pattern correlation of 0.54 (0.48) and a RSD of 1 (1.8) in winter (summer) for the P–ST (P–STn) correlation. The other is the MIROC5 model from MIROC with a pattern correlation of 0.1 (0) and a RSD of 1.3 (1) for the winter (summer) P–ST (P–STn) correlation.

Compared with the observed DJF precipitation–SST correlation and JJA precipitation–SST tendency correlation, which are shown in Fig. 1d and f, respectively, the HadCM3 model simulates the P–ST correlation well in winter. Similar to the observations, an opposite correlation is seen in the northern and southern SCS with a positive correlation of 0.3 in the northern SCS (Fig. 7a). The MIROC5 model shows a positive correlation over the whole SCS (Fig. 7b) so that the correlation in the southern SCS is opposite to the observed one. Such poor performance in the southern SCS is also identified in other models (e.g., IPSL-CM5A-MR). As for the summer, the P–STn correlation in

Fig. 7 Point-wise and simultaneous DJF precipitation–skin temperature correlation (*upper*) and JJA precipitation–skin temperature tendency correlation (*lower*) from **a**, **c** MOHC.HadCM3 and **b**, **d** MIROC.MIROC5. *Shaded regions* indicate that the correlations are statistically significant at the 90 % confidence level
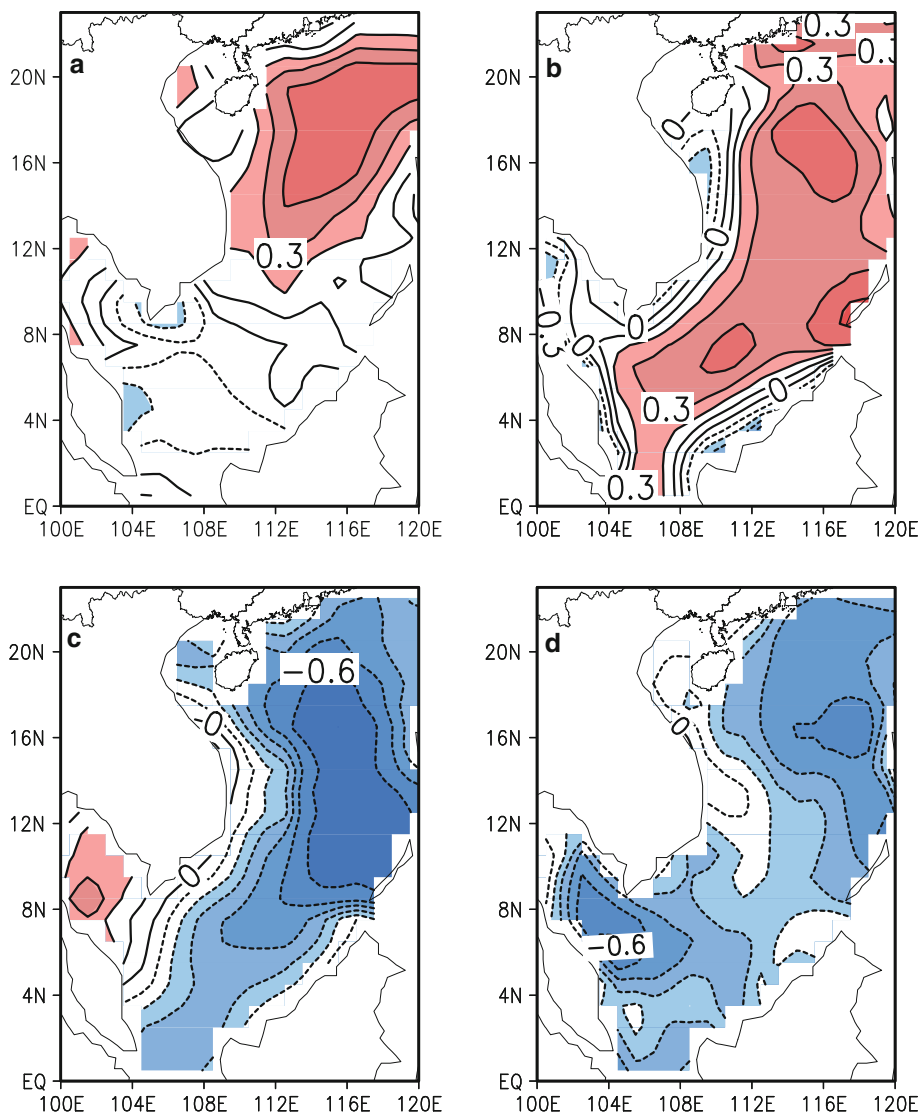
the HadCM3 model shows a same-sign distribution with a negative correlation center lying in central CSC (Fig. 7c), which is in accordance with the observations. In comparison, the negative correlation is somewhat overestimated, in particular, in the southern SCS. In contrast, the MIROC5 model has a poor simulation in the JJA P–STn correlation. Though the negative correlation is produced throughout the SCS, the distribution does not match with the observed one. The observation shows the largest precipitation–SST tendency correlation in the central SCS (Fig. 1f), while the MIROC5 displays a large negative correlation in both the northern SCS and the southwestern SCS, but a relatively weak correlation in the central SCS. The reasons for poor model performance may be related to the simulation of atmospheric response to remote forcing in the Pacific and Indian Oceans and the simulation of the regional oceanic processes. Further studies are needed to unravel the specific reasons for poor model performances.

6 Summary and discussions

The present study addresses the atmosphere–ocean interaction in interannual variations over the South China Sea and evaluates the performances of 24 selected models involved in CMIP5. The seasonality and regionality of the atmosphere–ocean relationship is demonstrated by comparing the simultaneous precipitation–SST and precipitation–SST tendency correlations. Distinct regimes of air–sea interaction are identified between summer and winter. An atmospheric forcing of ocean with a significantly negative precipitation–SST tendency correlation is dominant in the northern SCS and the central SCS from April to June, while an oceanic forcing of atmosphere with a significantly positive precipitation–SST correlation is identified in the northern SCS from November to December. These regimes of air–sea interaction are discussed by selecting two cases representing different processes in the SCS. During AMJ, the atmospheric forcing in the central SCS is characterized by remarkable cloud-radiation effects, wind-evaporation effects across the central basin, and wind-driven oceanic upwelling effects along the west coasts that contribute positively to the SST tendency anomalies in this region. The effects of ocean horizontal advection are unknown due to the low-resolution data. During NDJ, the regional convection responds to anomalous SST in the northern SCS due to modulation of the lower-level convergence associated with the large-scale circulation and the atmospheric stability.

Generally, the models simulate better the P–STn correlation than the P–ST correlation, which indicates that the models may be more capable of capturing the atmospheric forcing in the SCS. There are obvious differences of simulations among models in the same season with a wide range of spatial pattern correlation coefficients and standard deviations, and the performances of the same model are fairly unstable during different seasons. Most models have the worst performance in spring. Hence, improvement should be made in the models before the model simulations can be utilized to understand the regional air–sea interaction in the SCS.

The results obtained in the present study have both similarities and differences compared to previous relevant studies. The present study agrees with Xie et al. (2003) and Lestari et al. (2011) about the influence of atmospheric winds on SST changes during summer and with Wang et al. (2006a) about the importance of surface heat fluxes in the SST anomalies. For the southern SCS SST anomalies in winter, while Liu et al. (2004) emphasized the role of ocean advection, our analysis indicates the contribution of surface heat fluxes. Differing from Wang et al. (2006a), who focused on the processes for SST changes, we consider both the atmospheric influence on the SST anomalies and the SST forcing of the atmosphere. In addition, the present study evaluates the CMIP5 simulations in the SCS, which has not been done before.

It should be noted that the seasonality of the interannual atmosphere–ocean interaction may be related to the climatological field in the SCS. Wu and Kirtman (2007) pointed out that the dominance of atmospheric forcing or oceanic forcing is dependent on the mean state. Atmospheric forcing is likely prominent during warm and rainy season when the cloud-radiation effect is large. When surface heat flux changes induced by atmospheric process are small, the oceanic processes may contribute to the SST anomalies that, in turn, drive the atmospheric changes. Over the SCS, AMJ is the season of transition to the warm and rainy season. In this season, cloud starts to increase and wind disturbance is active. As such, the cloud-radiation effect and the wind-evaporation effect are large. In SON, the CSCS and the SSCS are still in the rainy season, and the cloud-radiation can induce an obvious atmospheric impact on the SST change.

In the present study, the oceanic forcing is only discussed qualitatively by considering the SST influence on the lower-level convergence and atmospheric stability. Verification of these processes should be made with proper model experiments in the future. As for the atmospheric forcing, due to the low-resolution data, the contribution of ocean advection needs further estimation. Moreover, the role of remote forcing is demonstrated to have impact on the development of both atmospheric and oceanic anomalies in the SCS (Klein et al. 1999; Qu et al. 2004; Wang et al. 2006b), and yet, in this study, we only consider the local forcing when discussing the regimes of regional atmosphere–ocean interaction in the SCS. The relative

roles of local forcing and remote forcing should be addressed in the future.

The evaluation of the model performance is preliminary for the purpose of understanding generally about how these models perform in revealing the regional air–sea relationship. The causes for good or poor model simulations are complicated and remain to be unraveled. Analysis in the future should further focus on what are the relative importance of regional processes and remote forcing in determining the model performance, which will provide guidance for improving the model capability of simulating properly the regional physical processes that connect the atmosphere and the ocean.

References

Adler RF, Huffman GJ, Chang A, Ferraro R, Xie P, Janowiak J, Rudolf B, Schneider U, Curtis S, Bolvin D, Gruber A, Susskind J, Arkin P, Nelkin E (2003) The Version 2 Global Precipitation Climatology Project (GPCP) monthly precipitation analysis (1979-Present). J Hydrometeor 4:1147–1167

Griffies SM, Harrison MJ, Pacanowski RC, Rosati A (2004) A Technical Guide to MOM4. GFDL Ocean Group technical report no. 5. NOAA/Geophysical Fluid Dynamics Laboratory, Princeton, p 342

He ZQ, Wu R (2013) Coupled seasonal variability in the South China Sea. J Oceanogr 69:57–69. doi:10.1007/s10872-012-0157-1

Huffman GJ, Adler RF, Bolvin DT, Gu G (2009) Improving the global precipitation record: GPCP Version 2.1. Geophys Res Lett 36: L17808. doi:10.1029/2009GL040000

Kanamitsu M, Ebisuzaki W, Woollen J, Yang SK, Hnilo JJ, Fiorino M, Potter GL (2002) NCEP-DOE AMIP-II Reanalysis (R-2). Bull Am Meteorol Soc 83:1631–1643

Klein SA, Soden BJ, Lau NC (1999) Remote sea surface temperature variations during ENSO: evidence for a tropical atmospheric bridge. J Clim 12:917–932

Lau NC, Nath MJ (2003) Atmosphere-ocean variations in the Indo-Pacific sector during ENSO episodes. J Clim 16(1):3–20

Lestari RK, Watanabe M, Kimoto M (2011) Role of air-sea coupling in the interannual variability of the South China Sea summer monsoon. J Meteor Soc Jpn 89A:283–290

Lindzen RS, Nigam S (1987) On the role of sea surface temperature gradients in forcing low-level winds and convergence in the tropics. J Atmos Sci 44:2418–2436

Liu QY, Jiang X, Xie SP, Liu WT (2004) A gap in the Indo-Pacific warm pool over the South China Sea in boreal winter: seasonal development and interannual variability. J Geophys Res 109:C07012. doi:10.1029/2003JC002179

Norris JR, Zhang Y, Wallace JM (1998) Role of low clouds in summertime atmosphere–ocean interactions over the North Pacific. J Clim 11:2482–2490

Paulson CA, Simpson JJ (1977) Irradiance measurements in the upper ocean. J Phys Oceanogr 7:952–956

Qu TD, Kim YY, Yaremchuk M et al (2004) Can Luzon strait transport play a role in conveying the impact of ENSO to the South China Sea? J Clim 17:3644–3657

Reynolds RW, Rayner NA, Smith TM, Stokes DC, Wang W (2002) An improved in situ and satellite SST analysis for climate. J Clim 15:1609–1625

Roxy M, Tanimoto Y (2007) Role of SST over the Indian Ocean in influencing the intraseasonal variability of the Indian summer monsoon. J Meteor Soc Jpn Ser II 85(3):349–358

Roxy M, Tanimoto Y (2012) Influence of sea surface temperature on the intraseasonal variability of the South China Sea summer monsoon. Clim Dyn 39(5):1209–1218

Taylor KE (2001) Summarizing multiple aspects of model performance in a single diagram. J Geophys Res 106(7):7183–7192

Taylor KE, Stouffer RJ, Meehl GA (2011) A summary of the CMIP5 experiment design. PCDMI Rep. from http://cmip-pcmdi.llnl.gov/cmip5/docs/Taylor_CMIP5_design.pdf. Accessed 22 Jan 2011

Taylor KE, Stouffer RJ, Meehl GA (2012) An overview of CMIP5 and the experiment design. Bull Am Meteorol Soc 4:485–498

Trenberth KE, Shea DJ (2005) Relationships between precipitation and surface temperature. J Geophys Res 32:L14703. doi:10.1029/2005GL022760

Twigt DJ, De Goede ED, Schrama EJO, Gerritsen H (2007) Analysis and modeling of the seasonal South China Sea temperature cycle using remote sensing. Ocean Dyn 57:467–484

Wang DX, Qin ZH, Zhou FX (1997) Study on air–sea interaction on the interannual time-scale in the South China Sea. Acta Meteorol Sin 55(1):33–42 (in Chinese)

Wang B, Wu R, Li T (2003) Atmosphere-warm ocean interaction and its impacts on the Asian-Australian monsoon variation. J Clim 16:1195–1211

Wang C, Wang W, Wang D, Wang Q (2006a) Interannual variability of the South China Sea associated with El Niño. J Geophys Res 111:C03023. doi:10.1029/2005JC003333

Wang DX, Liu Q, Huang RX, Du Y, Qu T (2006b) Interannual variability of the South China Sea through flow inferred from wind data and an ocean data assimilation product. Geophys Res Lett 33:L14605. doi:10.1029/2006GL026316

Wu R (2002) Processes for the northeastward advance of the summer monsoon over the Western North Pacific. J Meteor Soc Jpn 80(1):67–83

Wu R (2010) Subseasonal variability during the South China Sea summer monsoon onset. Clim Dyn 34(5):629–642

Wu R and Kinter III JL (2010) Atmosphere-ocean relationship in the midlatitude North Pacific: seasonal dependence and east–west contrast. J Geophys Res 115:D06101. doi:10.1029/2009JD012579

Wu R, Kirtman BP (2007) Regimes of seasonal air–sea interaction and implications for performance of forced simulations. Clim Dyn 29:393–410

Wu R, Kirtman BP (2011) Caribbean Sea rainfall variability during the rainy season and relationship to the equatorial Pacific and tropical Atlantic SST. Clim Dyn 37:1533–1550. doi:10.1007/s00382-010-0927-7

Wu R, Wang B (2000) Interannual variability of summer monsoon onset over the western North Pacific and the underlying processes. J Clim 13:2483–2501

Wu R, Wang B (2001) Multi-stage onset of the summer monsoon over the western North Pacific. Clim Dyn 17(4):277–289

Wu R, Kirtman BP, Pegion K (2006) Local air-sea relationship in observations and model simulations. J Clim 19:4914–4932

Wu R, Kirtman BP, Krishnamurthy V (2008) An asymmetric mode of tropical Indian Ocean rainfall variability in boreal spring. J Geophys Res 113:D05104. doi:10.1029/2007JD009316

Wu W, Wen ZP, Wu R, Wang TM (2011) Air-sea interaction over the subtropical North Pacific during the ENSO transition phase. J Clim 24:5772–5784

Wu R, Cao X, Chen W (2012) Surface wind speed-SST relationship during the passage of typhoons over the South China Sea. IEEE

Geosci Remote Sens Lett 9(5):933–937. doi:10.1109/LGRS.2012.2185819

Wu R, Chen JP, Wen ZP (2013) Precipitation-surface temperature relationship in the IPCC CMIP5 models. Adv Atmos Sci. doi:10.1007/s00376-012-2130-8

Xie SP, Xie Q, Wang D, Liu WT (2003) Summer upwelling in the South China Sea and its role in regional climate variations. J Geophys Res 108:3261. doi:10.1029/2003JC001867

Yu L, Jin X, Weller RA (2008) Multidecade global flux datasets from the Objectively Analyzed Air-sea Fluxes (OAFlux) Project: Latent and sensible heat fluxes, ocean evaporation, and related surface meteorological variables. Woods Hole Oceanographic Institution, OAFlux Project Technical Report. OA-2008-01, Woods Hole. Massachusetts